American Mineralogist, Volume 76, pages 113–127, 1991

The structure and origin of Fe-bearing platelets in metamorphic rutile

Jillian F. Banfield, David R. Veblen
Department of Earth and Planetary Sciences, Johns Hopkins University, Baltimore, Maryland 21218, U.S.A.

Abstract

High-resolution transmission electron microscopy has been used to characterize the defect microstructure of rutile from chlorite-, chloritoid-, garnet-, and staurolite-grade metapelites. Analytical electron microscopy (AEM) revealed that the rutile contained between 0.5 and 3 wt% FeO and that the Fe content generally increased with metamorphic grade. High-resolution images, nanoprobe-AEM analyses, and electron diffraction patterns indicated that the Fe is contained within platelets generally less than 1 nm wide that have the hematite structure. The regularly spaced platelets are coherently intergrown parallel to (100) and (010) of rutile. They closely resemble platelets reported from experimental studies of Ti^{3+}- and Fe-bearing rutile. We propose that the platelets in natural rutile are hematite and that apparent tripling of the {101} spacings results from dynamical diffraction. The hematite (or Ti_2O_3) structure represents an end-member arrangement of pairs of face-sharing octahedra. At higher temperatures in synthetic rutile these pairs are ordered to form crystallographic shear planes. We interpret the hematite platelets to have formed by a precipitation mechanism. This origin is consistent with the defect distribution and orientation and is supported by related experimental studies.

Introduction

This study describes the defect microstructure of Fe-bearing rutile from a range of low- and medium-grade metamorphic rocks. The investigation follows about 40 years of intensive research by numerous workers on synthetic rutile, including reduced, deformed, and Me^{3+}-substituted materials. Despite the attention devoted to synthetic rutile, little is known about nonstoichiometry in natural samples.

Electrical conductivity measurements (Baumard et al., 1977) indicate that there are three regions that exhibit different conductivity behavior in Ti^{3+}-bearing rutile: (1) a solid solution of TiO_{2-x} containing isolated point defects; (2) a two-phase mixture of TiO_{2-x} and Ti_nO_{2n-1}; and (3) a series of one- and two-phase regions of Ti_nO_{2n-1} (Smith et al., 1982). Marucco et al. (1981) and Gautron et al. (1981) demonstrate that over a range of temperatures and O partial pressures, regions exist in TiO_{2-x} where the predominant defects are (1) interstitial Ti, (2) doubly ionized O vacancies, and (3) O vacancies associated with charge compensation of trivalent impurities.

Numerous studies of synthetic rutile have used transmission electron microscopy (TEM) and electron diffraction to characterize a range of complex defect structures, including extended defects termed crystallographic shear planes (CSP), point defects, and platelets that develop in order to accommodate deviations from stoichiometry (e.g., Bursill and Hyde, 1972; Gibb and Anderson, 1972; Bursill, 1974; Blanchin et al., 1980; Smith et al., 1982; Bursill et al., 1982, 1983, 1984a, 1984b). Catlow and James (1982) calculated that the most stable defects are vacancies, which exist in equilibrium with shear planes. They attribute the stability of CSP to large stabilizing relaxations of the cations neighboring these planes. Blanchin et al. (1984, p. 364–366) reviewed the historical development of models for nucleation and growth of CSP.

Ordered structures with compositions Ti_nO_{2n-1} with $4 < n < 36$, termed Magnéli phases, or $(Ti,Fe)_nO_{2n-1}$, can be derived from the rutile structure by crystallographic shear. These structures are interpreted as regular intergrowths of (121) CSP and (011) antiphase boundaries (APB) (Bursill and Hyde, 1972; Miyano et al., 1983), and the CSP can adopt a variety of orientations and spacings to accommodate variations in composition. High-resolution transmission electron microscopy (HRTEM) studies at near-atomic resolution have made many contributions to our understanding of the roles of deformation and cooling rates on defect structures of nonstoichiometric rutile and on the extent of disorder in the defect distributions (Smith et al., 1982; Bursill et al., 1982, 1983, 1984a, 1984b; Blanchin et al., 1984; Otero-Diaz and Hyde, 1984). Smaller deviations from stoichiometry ($\bar{x} < \sim 0.03$) have been attributed to homogeneous solid solution of point defects in the rutile matrix (Baumard et al., 1977; Blanchin et al., 1980).

Bursill and Blanchin (1983) proposed a structural model for interstitial defects in which nonstoichiometry is accommodated by incorporation of trivalent Ti atoms in pairs of face-sharing octahedra, rather than in interstitial defects forming strings of three face-sharing octahedra.

* Present address: Department of Geology and Geophysics, 1215 W. Dayton Street, Madison, Wisconsin 53706, U.S.A.

0003–004X/91/0102–0113$02.00

Aggregation of pairs of face-shared octahedra produces CSP.

Although most experiments have been carried out on samples cooled from high temperatures (e.g., 1100 °C), results obtained from TiO_{2-x} samples annealed at lower temperatures and then quenched revealed a new type of platelet defect parallel to {100} (Smith et al., 1982; Bursill et al., 1983, 1984a, 1984b). Bursill et al. (1984a) suggest that aggregation of cation interstitial defects results in formation of either CSP or platelet defects, depending upon cooling history. The Ti^{3+}-bearing defects described by Bursill et al. (1984a) closely resemble the platelets described in our study of metamorphic rutile.

Putnis and Wilson (1978) and Putnis (1978) described hydrothermal Fe-bearing rutile (0.55 wt% FeO and 0.28 wt% V_2O_5) from quartz-rutile rocks. A TEM study of the rutile at about 1-nm resolution indicated that although the rutile contained no separate Fe-bearing phase, annealing at 475 and 595 °C resulted in the precipitation of two transitional phases before formation of hematite (Putnis, 1978). The first-formed precipitate (Tr-1) was coherent with the rutile matrix (no noticeable change in the rutile diffraction pattern), and was inferred to be Fe-rich. Putnis described the domains of this phase as Guinier-Preston zones. The second transitional phase (Tr-2) shared the rutile subcell; based on several diffraction patterns, Putnis selected a monoclinic unit cell with a = 0.546 nm, b = 0.459 nm, c = 0.887 nm, β = 122.8°. Putnis proposed that Tr-2 contains an additional Fe atom in every third (011) layer. Bursill et al. (1984a) pointed out that unlike ilmenite and hematite, Putnis' model contains infinite chains of face-sharing octahedra and that each (010) layer has the stoichiometry $[FeTi_3O_6]^{3+}$, with no allowance for charge compensation. Bursill et al. constructed alternative models that explain the repeat of 3 $\times$ d_{101} (rutile) observed in Tr-2 and Ti^{3+}-bearing synthetic rutile.

In the present study, we have detailed the structures and compositions of defects in rutile from a range of metamorphosed pelitic rocks. Our results from metamorphic rutile also suggested a monoclinic unit cell based on a repeat of 3 $\times$ d_{101} (rutile), differing from the unit cell of Putnis (1978) only in the length of b due to splitting of the rutile subcell reflection. We show, however, that these results can be better interpreted as resulting from dynamical diffraction involving finely intergrown hematite and rutile. Consequently, our interpretation of the diffraction characteristics and thus the structure of the platelet mineral differs significantly from Putnis' model for defects in artificially annealed Fe-bearing rutile. The models of Bursill et al. (1984a) for platelet defects parallel to {100} rutile contain corner- and edge-linked pairs of face-sharing octahedra. Hematite also contains pairs of face-sharing octahedra, and as such represents an ordered end-member case of the structures proposed by Bursill et al. The similarity between the defects in metamorphic rutile and those produced in controlled laboratory studies provides support for our interpretation of the lamellae in metamorphic rutile as precipitation products.

Experimental procedures

Crystals of rutile examined in this study occur in metapelite samples from two regions in Vermont. The first set of samples were chlorite- and chloritoid-grade slates from the Taconic Range, collected from roadcuts along Vermont Route 4 west of Rutland (sample numbers 2112 and 2113). Electron microscopy of chloritoid in these rocks was described by Banfield et al. 1989). The rutile in the Taconic rocks occurs as extremely fine needles (generally no more than 4 μm in length and less than 1 μm wide) subparallel to the foliation defined by muscovite, paragonite, and chlorite. The petrology has been described by Zen (1960).

The second set of samples (A1, 18, F165, 333, 561, 565, 625: Karabinos, 1981, 1984; Banfield et al., 1989) were garnet- and staurolite-grade schists from the Hoosac Formation on the east side of the Green Mountains anticlinorium, near Jamaica, Vermont. Rutile crystals (up to 30 μm long and 8 μm wide) occur as inclusions in chloritoid and coexist with ilmenite inclusions in garnet. In these metapelites rutile does not appear to be present in the sheet-silicate dominated matrix.

Electron-transparent foils were prepared for electron microscopy by ion milling 2.3-mm slices of rock removed from petrographic thin sections. Specimens were coated with C and examined with a Philips 420T transmission electron microscope (TEM) operated at 120 keV and a JEM 4000EX TEM operated at 400 keV. In samples where rutile crystals were contained in chloritoid or micas, the silicates thinned rapidly, leaving isolated peninsulas of rutile that could be readily located and examined without interference from the matrix (Fig. 1). HRTEM images were obtained from thin edges of crystals at close to Scherzer defocus (approximately 80 nm underfocus for the 420T and 48 nm underfocus for the 4000EX). Typically, images were recorded at magnifications between 105 000× and 490 000×.

Both selected-area and convergent-beam electron diffraction (SAED and CBED) patterns were used in this study to characterize the orientation, unit-cell parameters, and fine structure of intergrowths. Micro-CBED patterns were used to locate lamellae-rich regions for microanalysis. The micro-CBED patterns and microanalyses were obtained using the nanoprobe mode of the Philips 420, with an effective spot size estimated to be between 2 and 3 nm.

Dark-field images were obtained with the crystals oriented as closely as possible to two-beam diffracting conditions. A relatively small (10-μm) objective aperture was used to isolate small areas of the SAED pattern, so that images could be formed from superlattice reflections, streaks, and split reflections. Typically, the dark-field images were recorded at 60000× to 105 000×, using long exposure times.

Analytical electron microscope (AEM) X-ray analyses were obtained with an EDAX energy dispersive spectrometer (EDS) on the Philips 420 and reduced with a Princeton Gamma-Tech System IV analyzer. AEM procedures generally follow those described by Livi and Veblen (1987), Appendix 2. Bulk analytical data were obtained from platelet-bearing rutile using a relatively large spot size (~60 nm). Duplicate analyses were obtained from numerous crystals in random orientations, with count rates between 900 and 1300 cps over the 20-keV spectrum and counting times of 100–200 s. Qualitative microanalyses were obtained at very low count rates (<100 cps), over long counting times (up to 500 s), with a spot size of approximately 2–3 nm.

Results

Electron diffraction and imaging

Figure 1 illustrates a low-magnification [001]-zone image of a rutile crystal enclosed by phyllosilicates in a chloritoid-grade metapelite (sample 2113). Dark contrast indicates the presence of platelets in two orthogonal orientations parallel to (100) and (010) of rutile.

The [001]-zone images of rutile (sample 2113) indicate that the platelets are very narrow, generally only the equivalent of two rutile unit cells wide (Figs. 2a, 2b, 2c). Platelets are composed of discontinuous segments offset laterally by small distances, often one rutile unit cell (Fig. 2b). Rutile (110) fringes are offset up to one half of a unit cell across platelets (Fig. 2c). Distortion of the rutile due to the presence of platelets is indicated by considerable strain contrast (Fig. 2a) and variations in the orientation of the rutile adjacent to platelet margins (Fig. 2b).

The selected area electron diffraction (SAED) pattern for the [001] zone (Fig. 2d) contains both rutile subcell reflections (open arrows) and additional reflections (filled arrows). The additional reflections are weaker and are present adjacent to the 200 and 020 but not the 100 and 010 rutile reflections.

The SAED pattern from the [11$\bar{1}$] zone (Fig. 3; sample F165) shows considerable streaking of reflections that results from subdivision of the rutile by the irregularly spaced platelets. All SAED patterns from this zone (except one platelet-free crystal from a staurolite-grade metapelite discussed below) were characterized by the presence of superlattice reflections with a repeat of $3 \times d_{(101)}$. Apparent superperiodicities (moiré fringes, see below) are present in images perpendicular to the [011] and [101] directions.

Images from the [010] zone (Fig. 4a, specimen F165) illustrate narrow platelets approximately parallel to (100). Superperiodicities parallel to (101) and ($\bar{1}$01) are clearly visible (Fig. 4a), associated with superlattice reflections present in the SAED pattern (Fig. 4b).

Figures 3 and 4 illustrate the presence of sharp superlattice reflections corresponding to a repeat of $3 \times d_{(101)}$ developed in two orientations. However, when the rutile

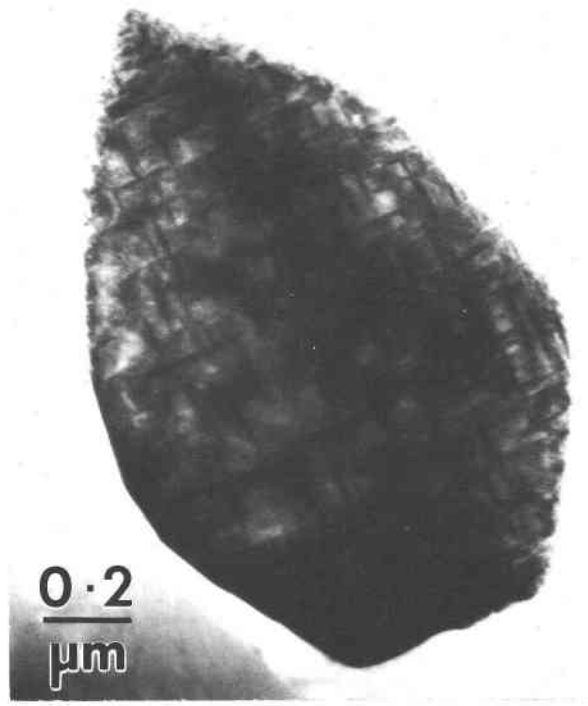

Fig. 1. Transmission electron micrograph of a rutile crystal from a chloritoid-grade metapelite (sample 2113), viewed down [001]. Platelets can be seen parallel to (100) and (010).

is viewed down [0$\bar{1}$2] as in Figure 5 (specimen 165), it can be seen that the superlattice reflections actually have a pencil-like shape. This indicates that the mineral producing these reflections forms crystals that are well ordered in two dimensions, but are probably no more than three unit cells wide in the third dimension. This is consistent with the high-resolution images of these platelets.

The SAED pattern from the [10$\bar{1}$] zone (Fig. 6a) shows splitting of all reflections except 010 and 101. Dark-field images were formed from a rutile substructure reflection (Fig. 6b) and from the additional reflection just inside it (Fig. 6c). The reflection used to form Figure 6c is illustrated in Figure 6d. The dark strips parallel to {010} in Figure 6b (arrowed) correspond with the regions diffracting strongly in Figure 6c (arrowed) and the platelets indicated by arrows in the bright-field image (Fig. 6e). These results indicate that splitting of reflections in electron diffraction patterns is due to the presence of narrow lamellae of a second mineral with a different reciprocal lattice.

A higher-magnification image of the [$\bar{1}$01] zone (Fig. 7a; sample F165) illustrates discontinuous lamellae parallel to (010). Microdiffraction (CBED) patterns were taken from the rutile matrix and from lamellae-rich regions (Figs. 7b, 7c). The 020 disks from rutile (Fig. 7b) indicate a spacing that is slightly smaller than the spacing from the lamella-rich region (Fig. 7c).

The [$\bar{1}$01] zone of rutile from sample 18 is illustrated in Figure 8. Bands of intensity in the lamellae can be seen

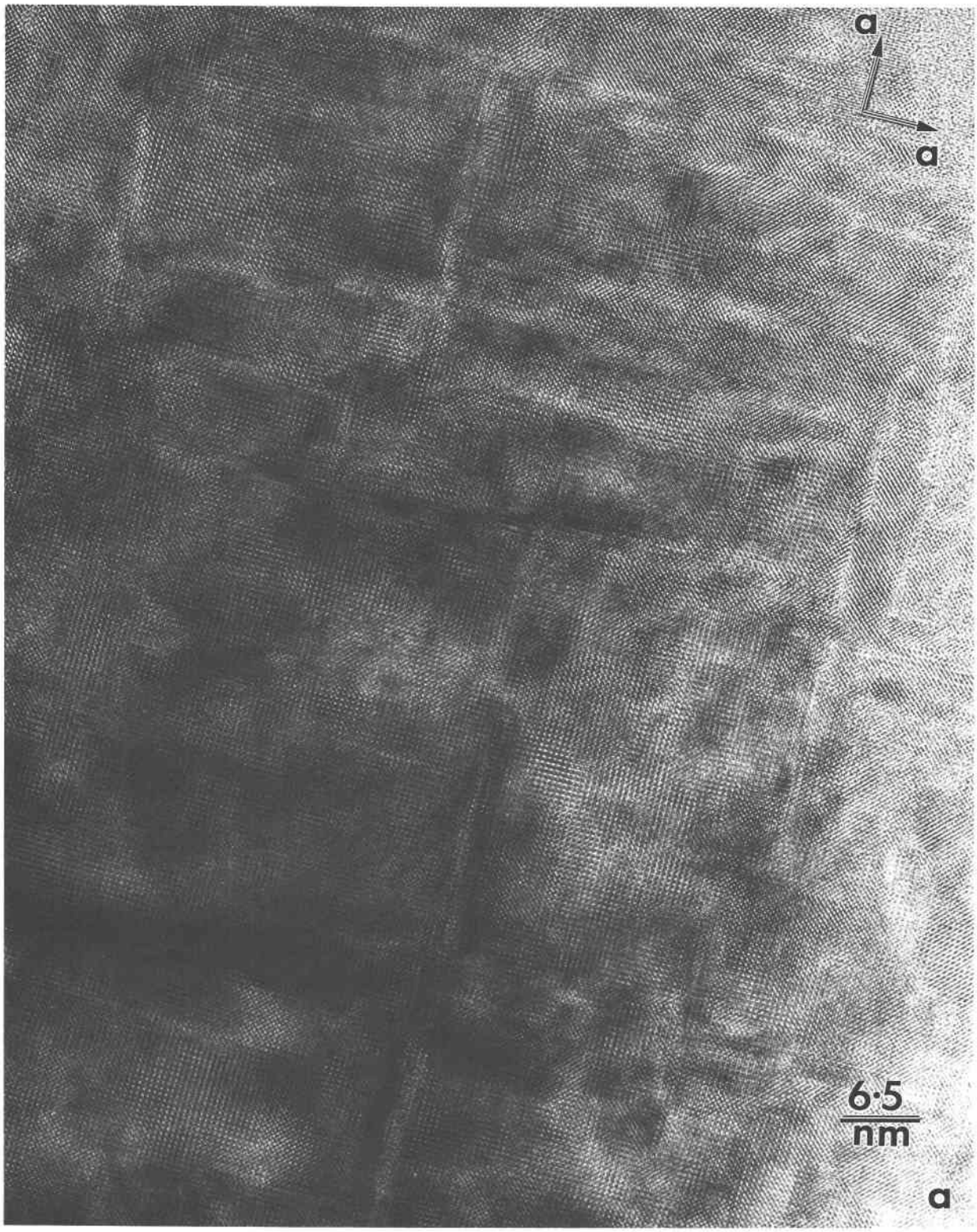

Fig. 2. (a) High-resolution images viewed down [001] of rutile (sample 2113) illustrating the presence of platelets parallel to (100) and (010) of rutile.

Fig. 2. (**b**) High-resolution images viewed down [001] of rutile (sample 2113) showing that platelets (P) are apparently ~1 nm wide.

perpendicular to the (010) lattice fringes of the rutile, indicating a superlattice associated with the mineral forming these platelets. The weakly developed periodic contrast inclined to (010) of rutile (a moiré pattern) is due to platelets parallel to (100) of rutile. Sample 18 contains more platelets than any other sample examined and has the highest, and most variable, Fe content (in excess of 3 wt% as FeO in some regions). This sample is unique in

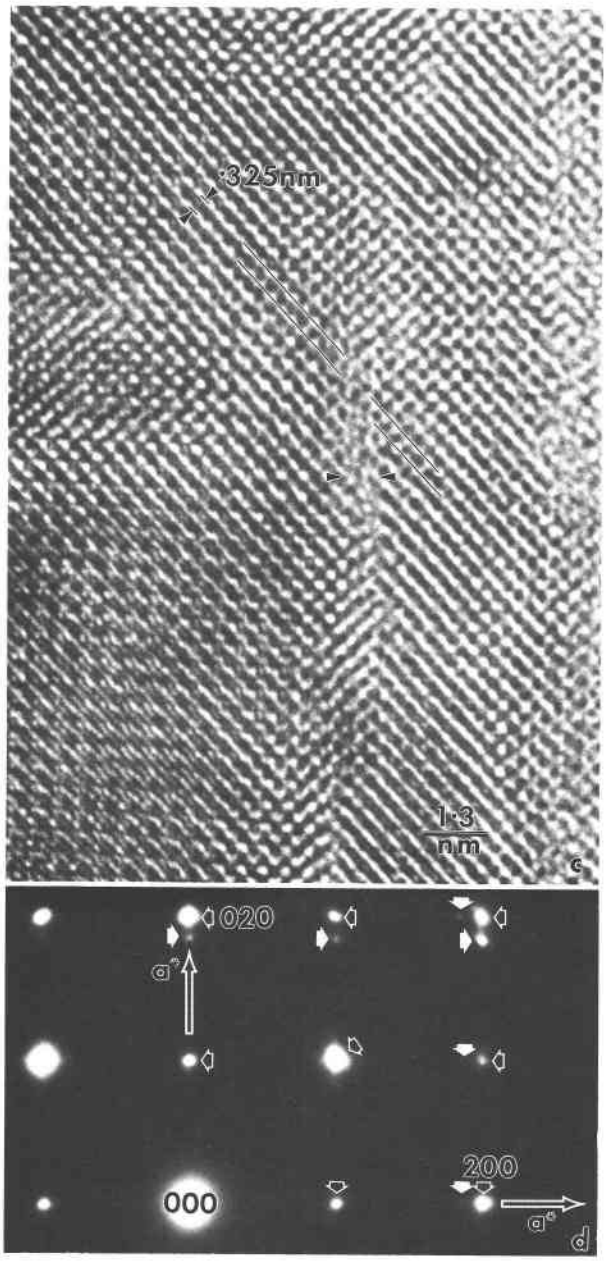

Fig. 2. (c) Image of rutile tilted fractionally from [001] showing a platelet (see arrows) that offsets rutile (110) fringes (sight along marked lines). (d) Part of the [001] SAED pattern showing splitting of the (200) and (020) rutile reflections (reflections arising from rutile shown by open arrows, additional reflections by white arrows).

Fig. 3. SAED pattern for [11$\bar{1}$] zone from rutile (sample 2112) illustrating the presence of a superlattice with a repeat of 3 × $d_{(101)}$, splitting of 1$\bar{1}$0 and $\bar{1}$10 rutile reflections, and pronounced streaking of subcell reflections.

that it is characterized by the unequal development of platelets parallel to the crystallographically equivalent (100) and (010) planes. This is illustrated clearly by the image down [001] of rutile (Fig. 9a) and by the SAED pattern (Fig. 9b) showing extra diffraction spots (arrowed) associated with only one of the two {100} directions. The extra reflections form a reciprocal lattice that is rotated relative to the orientation observed in all other samples.

Analytical electron microscopy

Average weight percent FeO determinations were obtained from the thin edges of rutile crystals from samples F165, 561, 18, 2112, and 2113. Results from each sample were highly variable. This almost certainly reflects variations in the abundance of lamellae in rutile. The estimated FeO contents for samples listed approximately in order of increasing metamorphic grade were 0.7 wt% for sample 2112, 0.8 wt% for sample 2113, 1.4 wt% for sample F165, about 1.6 wt% for sample 561, and very approximately 3 wt% for sample 18.

Microanalyses were obtained from very small regions of sample F165 containing several closely spaced lamellae (Fig. 10). CBED patterns were observed during analysis to ensure that the reciprocal lattice associated with the platelet mineral was dominant (e.g., Fig. 7c). Due to the narrow size of the platelets, it was not possible to analyze the platelet mineral alone; consequently the data in Figure 10 reflect variable contamination by the essentially Fe-free rutile. Considerable concentration of Fe in the lamellae is apparent, with enrichments commonly four times that of the bulk rutile plus lamellae (Fig. 10).

Abundance of lamellae in the rutile samples

Relatively low-magnification images (0.46-nm fringes just visible) were obtained with the electron beam parallel to [010] or [$\bar{1}$01] in order to estimate the abundance of lamellae in sample F165. This information, combined with the FeO content of the crystal, could indicate the composition of the lamellar mineral if the thickness of the Fe-enriched region was known accurately. As dis-

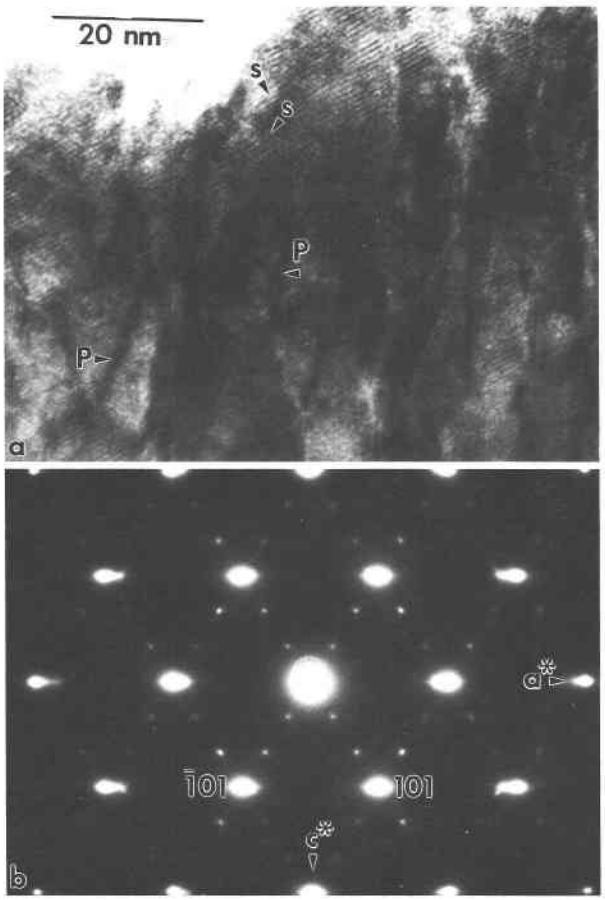

Fig. 4. (**a**) Image viewed down [010] of rutile (sample F165) illustrating discontinuous platelets (P) parallel to (100) and a weak superstructure (S) in two orientations parallel to (101) and ($\bar{1}$01) rutile; (**b**) SAED pattern for **a** showing very clear extra reflections.

cussed below, this approach did not produce an accurate lamellar composition. The results suggested sample F165 contains 3 to 6 vol% platelets (average of 4.5 vol%) in each orientation and thus approximately 9% by volume of the Fe-enriched mineral. It was estimated that the total volumetric concentration of platelets in sample 2112 was 5%; and in specimen 2113, 6%. The abundance of lamellae in sample 18 was estimated to be somewhat less than 18 vol%, but calculations were complicated by the unequal development of platelets parallel to (100) and (010) of rutile.

Only one of the metamorphic rutile crystals examined in this study did not contain lamellae (Fig. 11). This crystal was included in garnet from a staurolite-bearing sample (A1). The rutile crystal partially encloses an ilmenite crystal (close to end-member composition) and a magnetite crystal (at the ilmenite-rutile interface). Ilmenite is a common inclusion in all garnet crystals from the Hoosac schist; it characteristically contains magnetite crystals that range in size from a few nanometers to hundreds of nanometers.

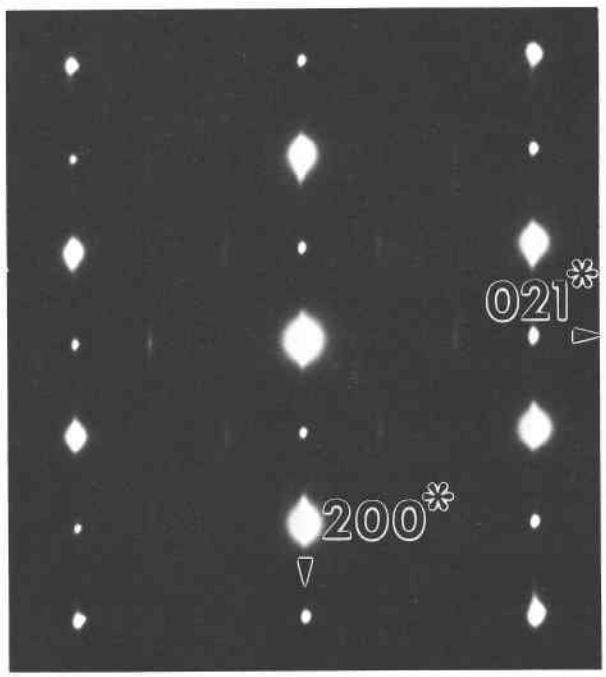

Fig. 5. SAED pattern viewed down [0$\bar{1}$2] (sample F165) illustrating elongate superlattice reflections.

Discussion

Electron diffraction, bright- and dark-field imaging, and X-ray microanalysis were used to study rutile crystals from metapelites from a range of metamorphic grades. These rutile crystals contain very narrow discontinuous platelets parallel to (100) and (010) of rutile (Fig. 2) that are Fe-enriched compared to the rutile host (Fig. 10). The spacing and widths of the lamellae vary to accommodate the variations in Fe content.

Mineralogic and crystallographic characterization of the intergrowths

The [001] zone of rutile illustrated in Figure 2d reveals the superposition onto the rutile diffraction pattern of two additional reciprocal lattices at 90° to each other, corresponding to the two platelet orientations. The lamellae share either $\mathbf{a}_1^*$ or $\mathbf{a}_2^*$ of rutile and have a second reciprocal lattice vector that is shorter than **a*** of rutile and at 90° to the first. If these directions are selected as **a*** and **b***, with **c*** defined by the apparent superlattice along the 101 reciprocal lattice row of rutile (Figs. 3, 4), then a monoclinic unit cell can be described with $a = 0.54$ nm, $b = 0.50$ nm, $c = 0.89$ nm, and $\beta = 122.5°$, similar to that selected by Putnis (1978) for his intermediate phase (Tr-2). However, it is also possible that the 0.75-nm superlattice reflection ($3 \times d_{101}$ of rutile) is introduced by dynamical diffraction involving the 0.37-nm reflection ($3/2 \times d_{101}$) and the 0.25-nm 101 rutile reflection. In this case, we can interpret the diffraction patterns as resulting from the superposition of zones from a rhombohedral

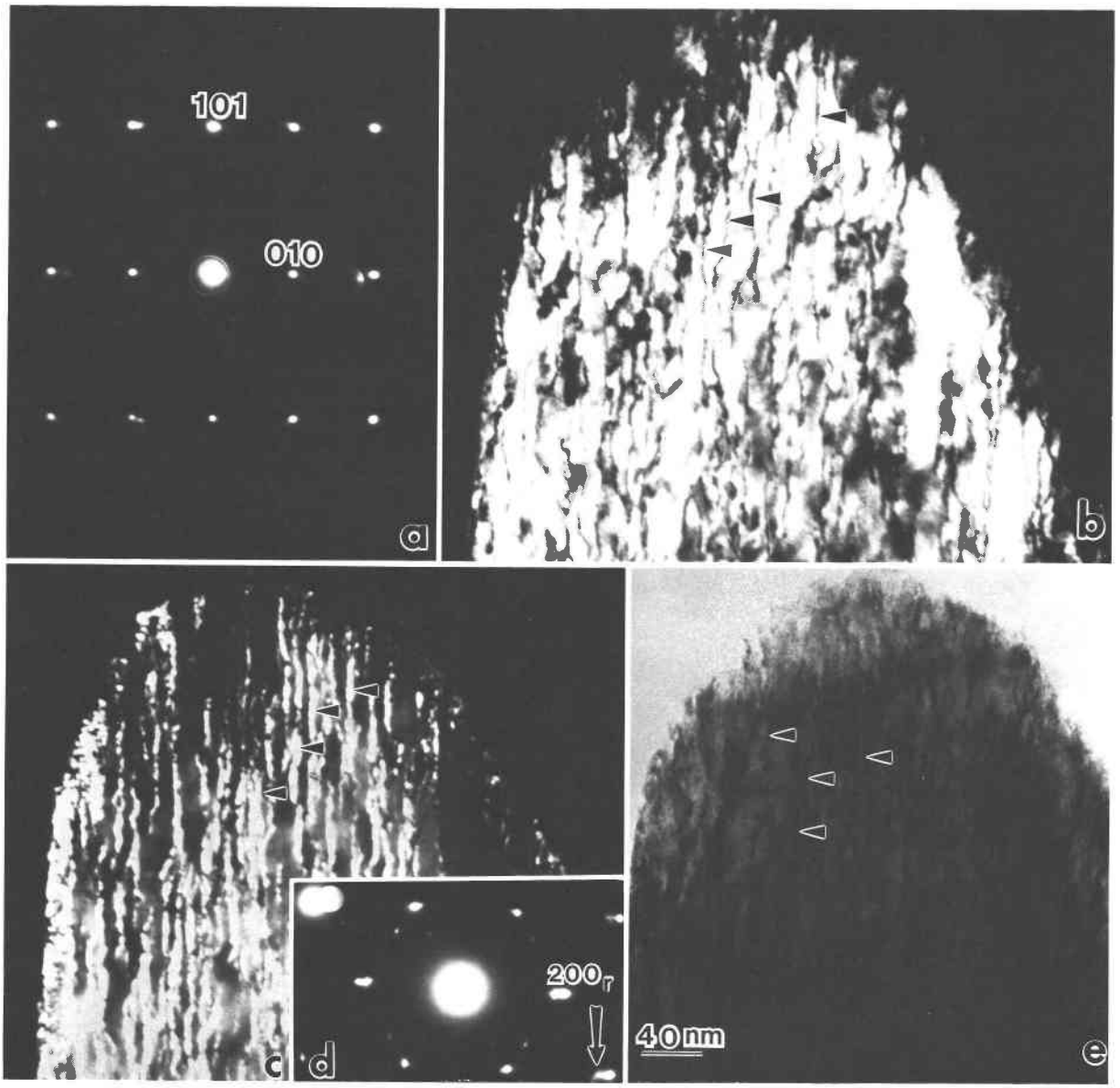

Fig. 6. (a) SAED pattern from [10$\bar{1}$] rutile (F165) showing splitting of subcell reflections; (b) dark-field image formed from rutile reflection; (c) dark-field image formed from additional reflection; (d) SAED pattern showing the reflection used to form the image in c (marked by image of an objective aperture); (e) bright-field image down [$\bar{1}$01]. Platelets are indicated by arrows.

oxide (ilmenite or hematite with d_{012} = 0.37 nm) and rutile.

The shape of the superlattice reflections in electron diffraction patterns (Fig. 5) and the dark-field images formed from split reflections clearly demonstrate that the superlattice arises from the mineral contained within the narrow platelets. Consequently, the [010] rutile electron diffraction pattern (Fig. 4) is logically interpreted in terms of the superposition of diffraction effects from rutile, from the narrow lamellae oriented edge-on (giving rise to streaky reflections), and from the lamellae that lie in the plane of the image (giving rise to the sharp reflections that trisect [101] rutile).

Figure 12 illustrates the individual diffraction patterns (Figs. 12a, 12b, 12c) that are superimposed to form the SAED pattern shown in Figure 4b and illustrated in Figure 12d. These include [010] rutile (Fig. 12b), the (twinned) [001] hematite zones (from lamellae parallel to (100) rutile; Fig. 12a), and (twinned) [100] hematite zones (from the lamellae parallel to (010) of rutile; Fig. 12c). Figure 13 shows a schematic diagram of the intergrowth. The diffraction pattern in Figure 12d results if the electron beam is vertical.

Figure 2c shows an offset of the rutile (110) fringes by approximately 0.5 × $d_{(110)}$ across the platelets. Figure 13 demonstrates that this could result from the presence of

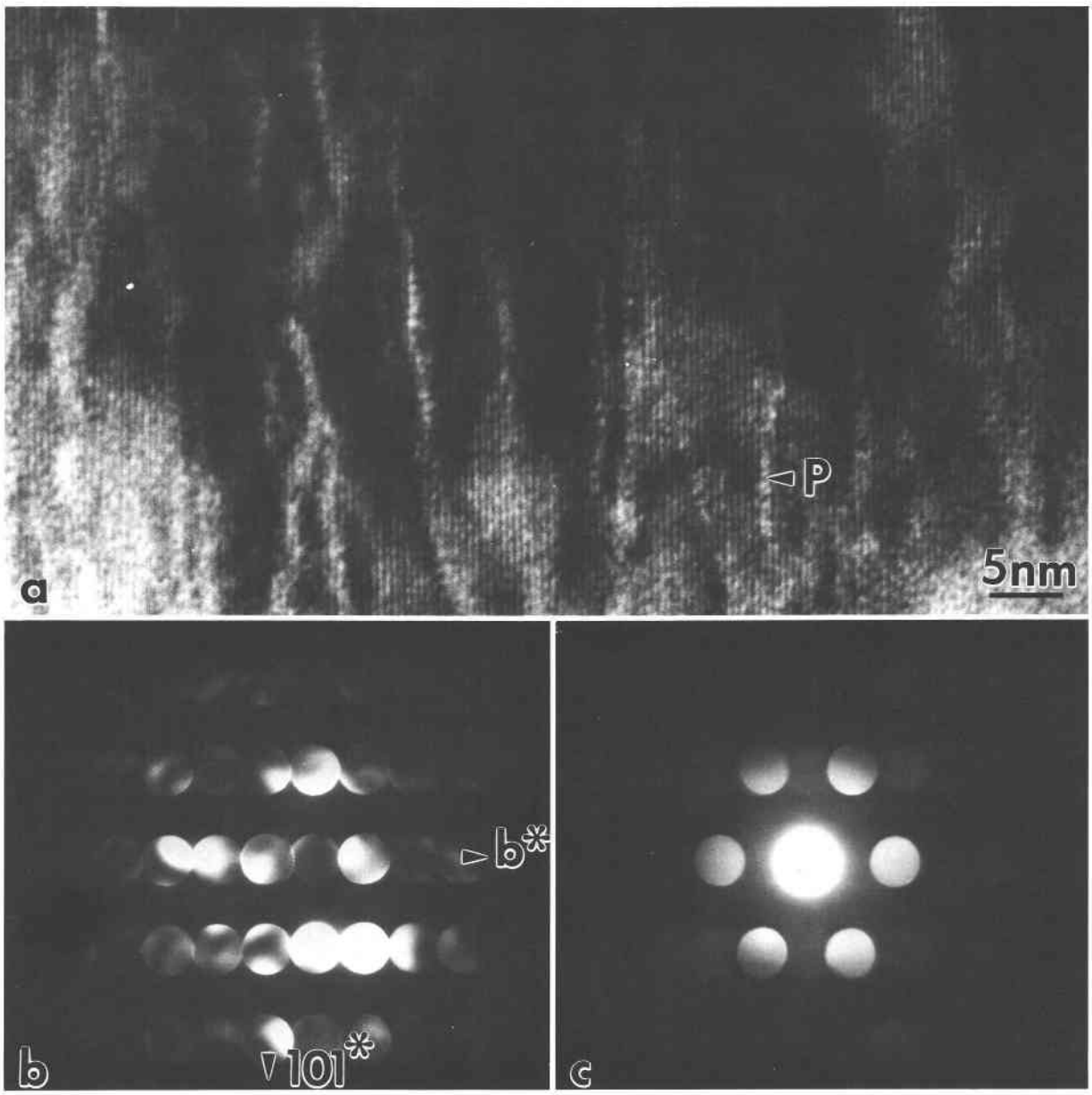

Fig. 7. (**a**) The [$\bar{1}$01] zone of rutile containing lamellae (P) parallel to (010). Micro-CBED pattern from rutile host (**b**) and from lamellae (**c**).

lamellae two unit cells wide within the rutile. The offset arises because the dimension perpendicular to the lamellae is larger than *a* of rutile, so that the offset of (110) fringes will vary with the width of the lamellae. Similar offsets were noted in some regions of high-resolution images of Ti^{3+}-bearing rutile by Bursill et al. (1984a), who proposed an alternative precipitation mechanism to explain platelets showing this phenomenon.

In his study of the phases produced by annealing Fe-bearing rutile, Putnis (1978) described twinning in an intermediate phase (Tr-2) and suggested that twinning reduces the overall strain energy of the precipitate-matrix interface by reducing the degree of misfit between the rutile and Tr-2. Electron diffraction patterns in this study are interpreted to indicate twinning of the platelets. The twin operation is a mirror parallel to (001) of the rhombohedral oxide; the labels on the **a** axes related by the mirror have been reversed on Figure 13 to satisfy the right-hand rule. Putnis (1978) noted that contrast in images of the intermediate phase is structure factor contrast, not strain contrast. He suggested a lamellar composition similar to that inferred in this study from the lamellar abundance and FeO content described below. Our images of lamellae in metamorphic rutile suggest that coherency strain is associated with the presence of the platelets, and this presumably contributes to the variable appearance

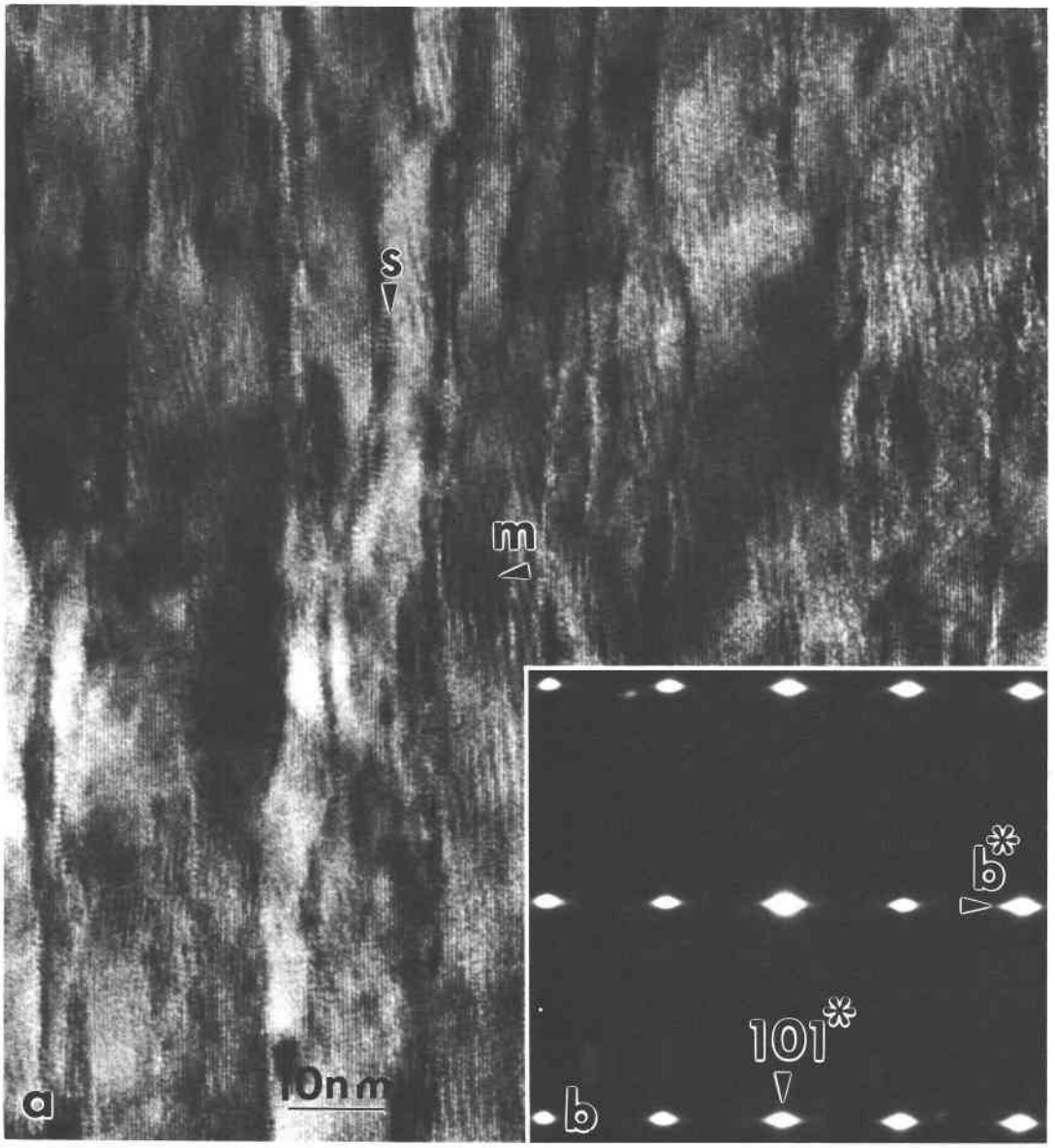

Fig. 8. (a) The [$\bar{1}$01] zone of rutile (sample 18) illustrating a superlattice (S) associated with the abundant lamellae. Moiré fringes (M) arise from the presence of inclined platelets; (b) corresponding SAED pattern.

of high-resolution images (e.g., in Fig. 2), as well as to the total contrast.

The composition of the lamellae

Using the rutile as an internal standard, we determined the *c*-dimension of the rhombohedral oxide to be approximately 1.38 nm. Plots of hexagonal cell dimensions vs. composition for ilmenite-hematite solid solutions (Lindsley, 1965) suggest a composition close to that of hematite, although this method of determination of composition may not be accurate for coherently intergrown lamellae that are generally no more than three unit cells wide. The absence of the 003 reflection in the [110] zone provides strong evidence for the identification of the mineral in the lamellae as hematite, or disordered ilmenite, rather than ilmenite. The 003 reflection (hexagonal cell setting) is absent in space group $R\bar{3}c$ but present in $R\bar{3}$ (ilmenite) due to ordering of Fe and Ti. As the stable rhombohedral oxides at low temperature are close to the end-member compositions, we suggest that the composition of the lamellae is probably close to Fe_2O_3. The presence of hematite rather than ilmenite, which is the oxide predicted to be stable on the basis of the inferred f_{O_2} of the metapelites containing rutile, chloritoid, and,

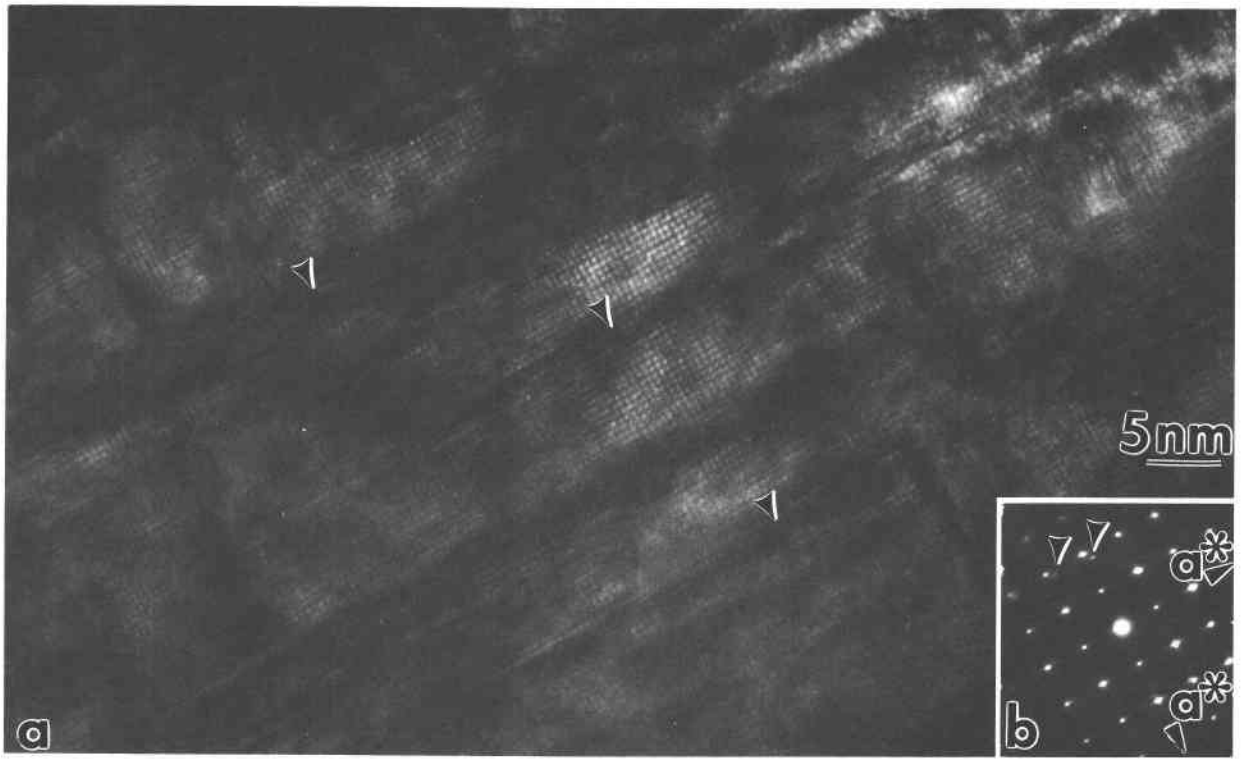

Fig. 9. (**a**) The [001] zone of rutile (sample 18) showing unequal development of lamellae (arrowed) parallel to (010) and (100) of rutile; (**b**) SAED pattern for **a** illustrating a slight rotation of the lattice of the lamellae (arrowed) relative to that of the rutile.

in the case of the Hoosac schists, ilmenite, suggests that the lamellae may have formed as a result of a late-stage oxidation event. As ilmenite has a closely related structure and a unit cell very similar to that of hematite, it is likely that under different conditions ilmenite could also form narrow lamellae in rutile.

The volumetric data and bulk FeO contents suggest that the platelet mineral has an Fe:Ti ratio of approximately 1:4. We have included this incorrect observation, even though we know that the maximum Fe:Ti ratio is 1:1, because it highlights the discrepancy that almost certainly arises in the estimates of platelet volumes. These volumes were greatly overestimated, partly because of the difficulty in determining the positions of the lamellar boundaries, i.e., in making the platelet vs. matrix distinction. Careful examination of the highest-resolution images of the intergrowths (Figs. 2b, 2c) illustrates this. In Figure 2c the platelet could be considered to be defined by the tips of the arrows, or to consist, as it apparently does, of only the narrow strip in the interior of this zone. In the lower-magnification images used in our volume measurements, strain contrast further increases the apparent widths of the lamellae.

Dependence of bulk composition on metamorphic grade

The rutile crystals from a variety of metapelites have Fe contents that show a positive correlation with metamorphic grade. This may reflect increased solid solution of Fe in the rutile structure, or possibly an increase in the interstitial defect concentration, with increase in temperature.

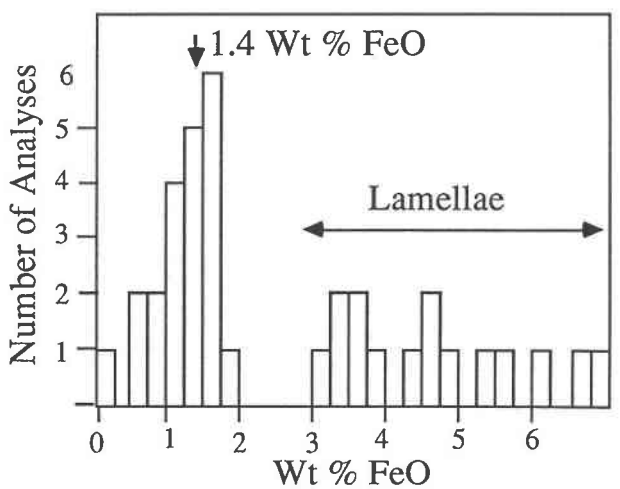

Fig. 10. Wt% FeO content vs. number of analyses for sample F165. Bulk lamellae + rutile has an average FeO content of 1.4 wt%, while microanalyses from lamellae-rich regions show considerable Fe enrichment.

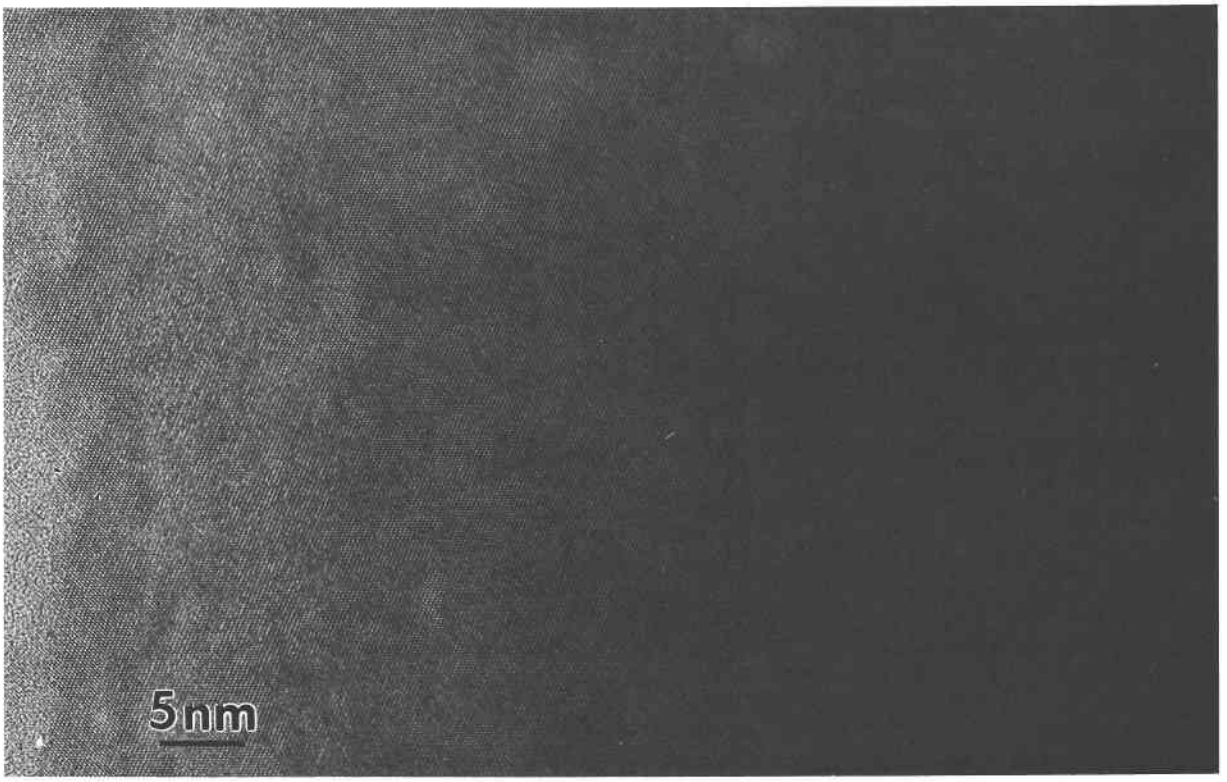

Fig. 11. A platelet-free rutile crystal (Al).

Further research is needed to determine whether the correlation between the Fe content of rutile and metamorphic grade is independent of whole-rock composition and other aspects of metamorphic history. The potential of such a correlation may be in its application as a geothermometer in rocks that have experienced temperatures less than 500 °C, where conventional geothermometers (e.g., Spencer and Lindsley, 1981) cannot be used.

Comparison with studies of synthetic rutile

The similarity in appearance of Ti^{3+}-bearing platelet defects (Bursill et al., 1984a) and those described here has already been noted. Bursill et al. recognized linear defect contrast parallel to {101} that is very similar to the linear contrast labeled "s" in Figure 4a.

Bursill et al. (1984a) proposed that models advanced to explain the precipitation of pairs of crystallographic shear planes (CSP) (Bursill and Blanchin, 1983; Blanchin et al., 1984) could be adapted to provide a more reasonable structure for the Tr-2 phase than that proposed by Putnis (1978), as well as the features observed in reduced rutile. The model of Bursill et al. requires that three Ti^{4+} are replaced by four Ti^{3+} cations, with the development of pairs of face-sharing octahedra, as are found in hematite (Bursill et al., 1984a).

Arrangements such as those described by Bursill et al. (1984a, their Figs. 13, 15, and 16) were designed to reproduce the superlattice with a repeat of $3 \times d_{(101)}$. If the tripling of {101} arises from dynamical diffraction involving the 012 hematite and 101 rutile reflection as we believe, the requirement for the complex arrangements shown by Bursill et al. is removed. The (121)-CSP models (Fig. 16 of Bursill et al., 1984a) can then be extended in an orderly manner to generate the hematite (or Ti_2O_3) structure, consistent with the identification of platelets with this structure in metamorphic rutile. Thus, extending the work of Bursill and coworkers, we can visualize trivalent cation substitution in the rutile structure in both natural and synthetic samples as resulting in the development of either strips (discontinuous in some cases) of the rhombohedral oxide structure (CSP or Wadsley defects) or planes of this structure (platelet defects).

The mechanism by which synthetic rutile accommodates Al substitution has been recently reported by Blanchin and Bursill (1989) and Bursill and Blanchin (1989). In addition to the presence of α-Al_2O_3 precipitates they note regions displaying a rutile superlattice with a repeat of $3 \times d_{(101)}$. They interpret this superperiodicity as evidence for a transitional structure intermediate between rutile and alumina (Blanchin and Bursill, 1989; Bursill and Blanchin, 1989). This tripling, which is apparent at the interface between the rutile and alumina precipitates, may be alternatively explained as a moiré effect analogous to that observed in this study.

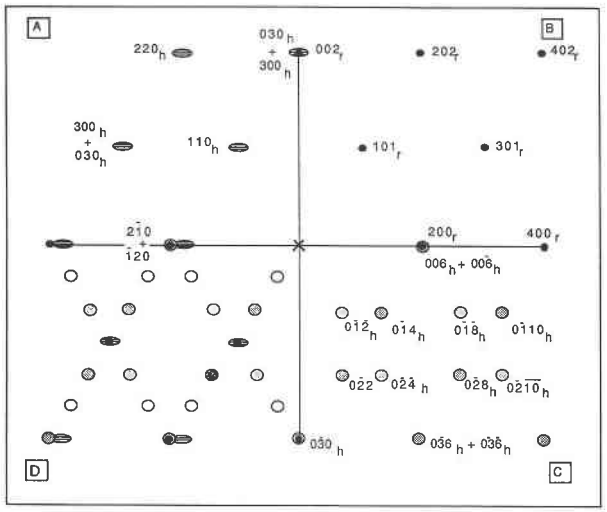

Fig. 12. Diagram illustrating the electron diffraction patterns from rutile and twinned platelets in two orientations: (**a**) [001] and [00$\bar{1}$] of hematite; (**b**) [010] of rutile; (**c**) [100] and [$\bar{1}$00] of hematite. The diffraction pattern resulting from the superposition of **a**, **b**, and **c** is illustrated in (**d**). Open circles indicate additional reflections resulting from dynamical diffraction.

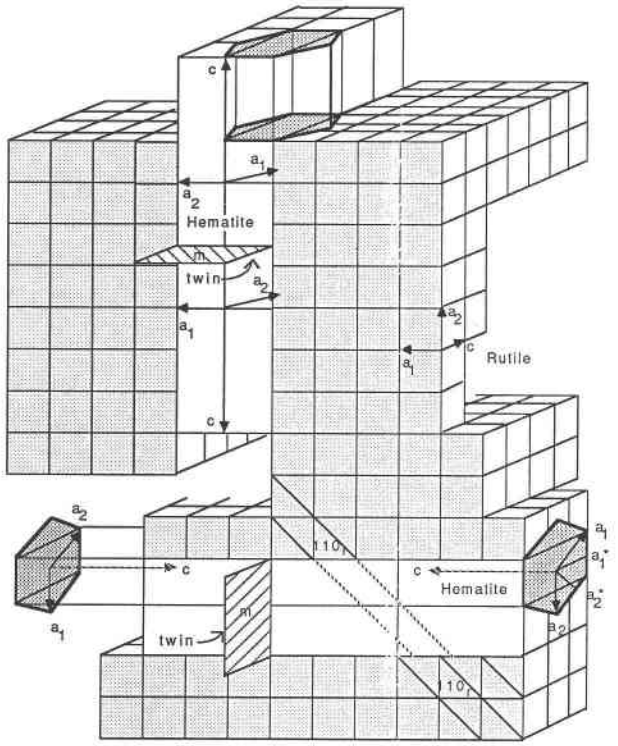

Fig. 13. Block diagram illustrating the intergrowth of twinned hematite platelets parallel to (100) and (010) of rutile. Solid lines labeled (110)$_r$ and their dotted extrapolations illustrate the offset of these planes evident in Figure 2c.

Nonstoichiometry in other minerals with the rutile structure

There are a number of other minerals that possess the rutile structure or its simple derivatives, including stishovite, cassiterite, pyrolusite, and marcasite. It will be interesting to discover whether lamellae with the rhombohedral oxide structure can accommodate nonstoichiometry in these oxides. Some evidence exists to indicate that similar defects do occur in pyrolusite. Rask and Buseck (1986) describe a phase M, which is characterized by a tripling along (101) in their [010] pyrolusite diffraction patterns (their Fig. 6). Rask and Buseck report that the sample contains no cations other than Mn, O, (and H), and they interpret the extra diffraction spots to indicate the presence of a new manganese oxide (hydroxide) mineral. A possible interpretation is that their pyrolusite contains platelets analogous to those reported here.

The origin of rutile in metapelites

Rutile typically occurs as needle-shaped crystals in the samples examined in this study. Within each sample, crystals appear to be fairly uniform in size, but they are smaller in the samples from the chlorite and chloritoid grades than in samples from the garnet and staurolite grades. Although the size variation may be explained in other ways, we interpret the needlelike, euhedral morphology and composition of the crystals to indicate that the rutile grew during metamorphism, rather than being detrital in origin.

It cannot be assumed that rutile in the Hoosac Formation garnet-, staurolite-, and kyanite-bearing samples grew by the same mechanism as rutile in the greenschist-facies rocks. In the higher-grade samples, rutile and Fe-Ti oxide crystals exist within garnet, but rutile is not present in the sheet-silicate-dominated groundmass. Rutile is present in the chlorite- and chloritoid-grade samples, although Goldsmith and Force (1978) suggest that it is typically not reported until much higher grades (e.g., kyanite grade). Goldsmith and Force (1978) suggest that the apparently uncharacteristic early appearance of rutile in the Taconic samples may be due to the unusual composition of these rocks. Alternatively, their view that rutile is restricted to higher-grade samples may simply reflect the fact that very small crystals would be overlooked by techniques other than TEM.

Thompson (1972) proposed that in metapelites the stability field for rutile increases at the expense of ilmenite with increasing grade. Blattner (1976) suggested that rutile crystals within garnet form from Ti released as garnet grows by consuming ilmenite. These considerations suggest that the coexistence of ilmenite and rutile in garnet reflects the incomplete consumption of ilmenite during prograde metamorphism. As no ilmenite or garnet is present in the greenschist-facies rocks, we presume that the rutile formed via another mechanism. A precursor mineral has not yet been identified, but it seems likely that finely crystalline TiO_2 (e.g., anatase or brookite) may have been present.

Rutile is the stable polymorph of TiO_2 over most or all of the range of geologically important conditions (Dachille et al., 1962; Post and Burnham, 1986) and is found in igneous, metamorphic, and sedimentary rocks. The abundance of precipitated oxides in rutile crystals may therefore be useful in determining the provenance of detrital rutile crystals in sedimentary rocks and placer deposits, for example.

The origin of platelets in rutile

There are two mechanisms that might cause the formation of the regularly spaced, Fe-rich lamellae in rutile: (1) periodic growth of hematite during the growth of the rutile, and (2) precipitation, or oxidation of Fe and precipitation within the rutile. This second mechanism must involve diffusion of Fe to fairly regularly spaced zones in the structure, where ordering of cations produces the narrow strips of rhombohedral oxide structure. We strongly argue for an origin due to precipitation from Fe-rich rutile for the platelets, rather than interpreting them as primary growth features. The reasoning is as follows:

1. Unusual conditions resulting in the periodic coprecipitation of Fe-enriched lamellae could be invoked to explain the development of platelets in rutile crystals from one locality, but it is difficult to believe that such conditions are normally encountered during crystallization of rutile by different reaction mechanisms, in a range of metamorphic grades, and from separate localities.

2. The correlation between Fe content and metamorphic grade suggests, not surprisingly, that Fe solubility in rutile is a function of temperature. It is difficult to explain this observation if Fe is never in solid solution in the rutile.

3. Experimental work of Bursill and coworkers described above has established that platelet defects with characteristics very closely resembling those described here form by aggregation of pairs of cations that are randomly distributed throughout the rutile at very high temperatures.

4. The platelets adopt distinct, symmetrically related crystallographic orientations that correspond to the low-temperature minima in Young's modulus (Bursill et al., 1978; Bursill et al., 1984a). As noted by Bursill et al., (1978) the (100) habit is favored for precipitation at these temperatures.

Conclusions

1. We have documented the presence of narrow lamellae in metamorphic rutile from metapelites that experienced a wide range of peak metamorphic temperatures. The data are consistent with the identification of the lamellar mineral as hematite (or ilmenite). These lamellae are generally one or two unit cells wide, and may thus be viewed as extended defects of rhombohedral oxide structure in rutile. Variations in Fe content of the bulk rutile are accommodated by increased thickness and abundance of the lamellae.

Our observations are similar in many respects to those reported previously for experimentally annealed Fe-bearing rutile (Putnis, 1978) and for synthetic, Ti^{3+}-bearing rutile (Bursill et al., 1984a). However, subtle but important differences were noted in the diffraction patterns in this study, most importantly, that the rutile subcell is not shared. The results suggest that nonstoichiometry in both natural and synthetic rutile may be explained by the presence of defects with the hematite structure.

2. The development of the lamellae throughout the rutile crystals in structurally reasonable orientations, the correlation between Fe content and metamorphic grade, and the regularity in size and shape of the platelets strongly suggest that the rutile is metamorphic in origin and that the lamellae are formed by expulsion of Fe originally present in the rutile structure. The similarities between these defects and Ti^{3+}-bearing platelets produced under controlled experimental conditions by previous workers support a retrograde precipitation origin for the platelets. The results from a range of metapelites suggest that precipitation of hematite is extremely common in metamorphic rutile.

Acknowledgments

We thank David Smith, Dimitri Sverjenski, Donald Miser, and James Rask for helpful discussions and reviews. The present research was supported by NSF grants EAR-8609277 and EAR-8903630. Electron microscopy was performed at the Johns Hopkins EM laboratory, which was established with partial funding from NSF grant EAR-8300365, and at the National Facility for High Resolution Electron Microscopy at Arizona State University, which is supported by NSF Grant DMR-8611609. We are grateful to David Smith for assistance with recording high-resolution electron micrographs at the ASU facility.

References cited

Banfield, J.F., Karabinos, P., and Veblen, D.R. (1989) Transmission electron microscopy of chloritoid: Intergrowth with sheet silicates and reactions in metapelites. American Mineralogist, 74, 549–564.

Baumard, J.F., Panis, D., and Anthony, A.M. (1977) Study of Ti-O system and TiO_2 at high-temperature by means of electrical-resistivity. Journal of Solid State Chemistry, 20, 43–51.

Blanchin, M.G., and Bursill, L.A. (1989) Non-classical twinning of alumina precipitates in rutile. Philosophical Magazine A 60, 619–630.

Blanchin, M.G., Faisant, P., Picard, C., Exxo, M., and Fontaine, G. (1980) Transmission electron microscope observations of slightly reduced rutile. Physica Status Solidi, A 60, 357–364.

Blanchin, M.G., Bursill, L.A., and Smith, D.J. (1984) Precipitation phenomena in non-stoichiometric oxides I. Pairs of crystallographic shear planes in reduced rutiles. Proceedings of the Royal Society of London, A 391, 351–372.

Blattner, P. (1976) Replacement of hornblende by garnet in granulite facies assemblages near Milford Sound, New Zealand. Contributions to Mineralogy and Petrology, 55, 181–190.

Bursill, L.A. (1974) An electron microscope study of the FeO-Fe_2O_3-TiO_2 system and of the nature of iron-doped rutile. Journal of Solid State Chemistry, 10, 72–94.

Bursill, L.A., and Blanchin, M.G. (1983) Structure of interstitial defects in non-stoichiometric rutile. Journau de Physique Letters, 44, L-165–L-170.

——— (1989) Interphase structures observed as alumina precipitates in rutile. Philosophical Magazine A 60, 631–642.

Bursill, L.A., and Hyde, B.G. (1972) Crystallographic shear in the higher Ti oxides: Structure, texture, mechanisms and thermodynamics. In H. Reiss and J.O. McCaldin, Eds., Progress in Solid State Chemistry, 7, p. 177–253. Pergamon Press, Oxford.

Bursill, L.A., Netherway, D.J., and Grey, I.E. (1978) Composition waves

in iron-doped rutile and the relationship between Young's modulus minima and crystallographic shear orientations. Nature, 272, 405–410.

Bursill, L.A., Blanchin, M.G., and Smith, D.J. (1982) The nature and extent of disorder within rapidly cooled $TiO_{1.9985}$. Proceedings of the Royal Society of London, A 384, 135–155.

Bursill, L.A., Blanchin, M.G., and Abdelmalek Mebarek (1983) Point, linear and extended defect structures in nonstoichiometric rutile. Radiation Effects, 74, 253–265.

Bursill, L.A., Blanchin, M.G., and Smith, D.J. (1984a) Precipitation phenomena in non-stoichiometric oxides II. {100} Platelet defects in reduced rutiles. Proceedings of the Royal Society of London, A 391, 373–391.

Bursill, L.A., Shen, G.J., Smith, D.J., and Blanchin, M.G. (1984b) Emergence of small defect contrast within HREM images of nonstoichiometric rutile. Ultramicroscopy, 13, 191–204.

Catlow, C.R.A., and James, R. (1982) Disorder in TiO_{2-x}. Proceedings of the Royal Society of London, A 384, 157–173.

Dachille, F., Simons, P.Y., and Roy, R. (1962) Pressure-temperature studies of anatase, brookite, rutile, and TiO_2 (II). American Mineralogist, 53, 1929–1939.

Gautron, J., Marucco, J.F., and Lemasson, P. (1981) Reduction and doping of semiconducting rutile (TiO_2). Materials Research Bulletin, 16, 575–580.

Gibb, R.M., and Anderson, J.S. (1972) Electron microscopy of solid solutions and crystallographic shear structures II. Fe_2O_3-TiO_2 and Ga_2O_3-TiO_2 systems. Journal of Solid State Chemistry, 5, 212–225.

Goldsmith, R., and Force, E.R. (1978) Distribution of rutile in metamorphic rocks and implications for placer deposits. Mineralum Deposita, 13, 329–343.

Karabinos, P. (1981) Deformation and metamorphism of Cambrian and Precambrian rocks on the east limb of the Green Mountains anticlinorium near Jamaica, Vermont. Ph.D. thesis, Johns Hopkins University, Baltimore, Maryland.

——— (1984) Deformation and metamorphism on the east side of the Green Mountain massif in southern Vermont. Geological Society of America Bulletin, 95, 584–593.

Lindsley, D.H. (1965) Iron-titanium oxides. Carnegie Institution of Washington Year Book, 64, 144–148.

Livi, K.J.T., and Veblen, D.R. (1987) "Eastonite" from Easton, Pennsylvania: A mixture of phlogopite and a new form of serpentine. American Mineralogist, 72, 113–125.

Marucco, J.F., Gautron, J., and Lemasson, P. (1981) Thermogravimetric and electrical study of nonstoichiometric titanium dioxide TiO_{2-x} between 800 and 1100 °C. Journal of the Physical Chemistry of Solids, 42, 363–367.

Miyano, T., Iwanishi, M., Harada, T., Kaito, C., and Shiojiri, M. (1983) A (110) CS structure in reduced rutile crystals. Philosophical Magazine, A 48, 163–167.

Otero-Diaz, L.C., and Hyde, B.G. (1984) A high-resolution electron microscopy study of disorder in two types of rutile-related crystallographic-shear phases. Acta Crystallographica, B 40, 237–244.

Post, J.E., and Burnham, C.W. (1986) Ionic modelling of mineral structures and energies in the electron gas approximation: TiO_2 polymorphs, quartz, forsterite, diopside. American Mineralogist, 71, 142–150.

Putnis, A. (1978) The mechanism of exsolution of hematite from natural iron-bearing rutiles. Physics and Chemistry of Minerals, 3, 183–197.

Putnis, A., and Wilson, M.M. (1978) A study of iron-bearing rutiles in the paragenesis TiO_2-Al_2O_3-P_2O_5-SiO_2. Mineralogical Magazine, 42, 255–263.

Rask, J.H., and Buseck, P.R. (1986) Topotactic relations among pyrolusite, manganite, and Mn_5O_8: A high resolution transmission electron microscopy investigation. American Mineralogist, 71, 805–814.

Smith, D.J., Blanchin, M.G., and Bursill, L.A. (1982) High resolution imaging of reduced rutiles. Micron, 13, 245–246.

Spencer, K.J., and Lindsley, D.H. (1981) A solution model for coexisting iron-titanium oxides. American Mineralogist, 66, 1189–1202.

Thompson, J.B., Jr. (1972) Oxides and sulfides in regional metamorphism in pelitic schists. 24th International Geological Congress, 10, 27–35.

Zen, E-an (1960) Metamorphism of the Lower Paleozoic rocks in the vicinity of the Taconic Range in west-central Vermont. American Mineralogist, 45, 129–175.

MANUSCRIPT RECEIVED JANUARY 10, 1990
MANUSCRIPT ACCEPTED NOVEMBER 10, 1990